ACS APPLIED MATERIALS & INTERFACES

www.acsami.org

Research Article

In Situ Evolution of Secondary Metallic Phases in Off-Stoichiometric ZrNiSn for Enhanced Thermoelectric Performance

Kishor Kumar Johari, Durgesh Kumar Sharma, Ajay Kumar Verma, Ruchi Bhardwaj, Nagendra S. Chauhan, Sudhir Kumar,* Manvendra Narayan Singh, Sivaiah Bathula, and Bhasker Gahtori*

Cite This: https://doi.org/10.1021/acsami.2c03065

Read Online

ABSTRACT: The full-Heusler (FH) inclusions in the half-Heusler (HH) matrix are a well-studied approach to reduce the lattice thermal conductivity of ZrNiSn HH alloy. However, excess Ni in ZrNiSn may lead to the in situ formation of FH and/or HH alloys with interstitial Ni defects. The excess Ni develops intermediate electronic states in the band gap of ZrNiSn and also generates defects to scatter phonons, thus providing additional control to tailor electronic and phonon transport properties synergistically. In this work, we present the implication of isoelectronic Ge-doping and excess Ni on the thermoelectric transport of ZrNiSn. The synthesized $ZrNi_{1.04}Sn_{1-x}Ge_x$ (x = 0−0.04) samples were prepared by arc-melting and spark plasma sintering and were extensively probed for microstructural analysis. The in situ evolution of minor secondary phases, i.e., FH, Ni−Sn, and Sn−Zr, primarily observed post sintering resulted in simultaneous optimization of the electrical power factor and lattice thermal conductivity. A *ZT* of ∼1.06 at ∼873 K was attained, which is among the highest for Hf-free ZrNiSn-based HH alloys. Additionally, ab initio calculations based on density functional theory (DFT) were performed to provide comparative insights into experimentally measured properties and understand underlying physics. Further, mechanical properties were experimentally extracted to determine the usability of synthesized alloys for device fabrication.

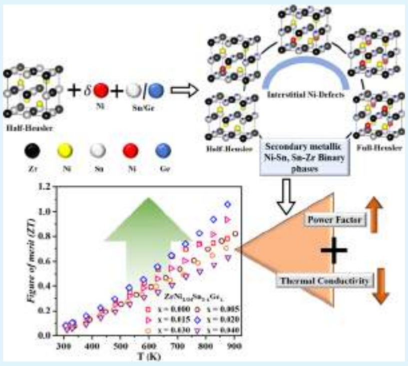

KEYWORDS: *thermoelectric, half-Heusler, off-stoichiometric, phonon dispersion, SPB model*

1. INTRODUCTION

Thermoelectric (TE) technology offers the interconversion of electrical and heat energy using solid-state devices. The TE efficacy of materials is determined via the figure of merit, $ZT = S^2\sigma T/\kappa$, where S is the Seebeck coefficient and σ is the electrical conductivity, which both cumulatively express the power factor, $\alpha = S^2\sigma$, while κ represents the thermal conductivity. In the last decade, many efforts have been devoted to developing materials with a high figure of merit. However, the practical applications of these materials have been limited due to the poor thermal stability, mechanical strength, etc.[1]

Ternary XYZ half-Heusler (HH) alloys have attained considerable interest due to their good electronic and mechanical performance, and these alloys are also thermally and chemically stable.[1,2] Here, X (Zr, Hf, Ti, etc.) and Y (Ni, Co, etc.) atoms are the transition or rare-earth metals; however, the Z (Sn, Sb, etc.) atom is the p-block element.[3,4] These HH alloys have a *MgAgAs*-type structure (space group $F\overline{4}3m$), and the Wyckoff positions occupied by the elements are as follows: X, 4a (0 0 0); Y, 4b (1/4 1/4 1/4); and Z, 4c (1/2 1/2 1/2); however, 4d (3/4 3/4 3/4) is vacant.[3,4] However, in XY_2Z full-Heusler (FH) alloys, the X and Z elements occupy the 4a and 4c sites, respectively, and the Y element occupies the 4b as well as 4d sites completely, which forms a $MnCu_2Al$-type structure (space group $Fm\overline{3}m$) with the X, Y, and Z atoms positioned at 4a (0 0 0), 8c (1/4 1/4 1/4), and 4b (1/2 1/2 1/2), respectively.[4]

Among HH alloys, ternary MNiSn (M = Hf, Zr, Ti)-based materials have been widely explored as *n*-type thermoelectric materials for mid-temperature range applications.[1] In general, Hf-containing MNiSn-based HH alloys have a lower thermal conductivity in comparison to Hf-free alloys. But Hf is relatively expensive and more toxic.[5] Therefore, various strategies like doping,[6−8] nanostructuring,[9] nanoinclusion/nanocomposite,[10,11] and so on have been adopted to reduce the thermal conductivity of Hf-free and half-Heusler alloys. Recently, the strategy of off-stoichiometry ($Ni_{1+\delta}$ ($0 < \delta < 1$))

Received: February 18, 2022
Accepted: April 6, 2022

in MNiSn has emerged as an effective way to reduce the thermal conductivity with simultaneous enhancement in the electronic transport properties of MNiSn-based HH alloys.[10,12−15]

The strategy of self-doping (off-stoichiometry) as $Ni_{1+\delta}$ ($0 < \delta < 1$) in MNiSn has two aspects, either excess Ni completely occupies the 4d site, which will induce the FH phase in the HH matrix, and/or it will partly fill the 4d site, which will induce interstitial Ni defects.

Do et al.[16] have predicted via ab initio calculations that excess Ni exhibits an attractive interaction with each other and comes closer to form nanoclusters in the ZrNiSn-HH matrix. Makongo et al.[14] have shown that FH nanoinclusion in the bulk HH matrix, which simultaneously increased the Seebeck coefficient and electrical conductivity, led to enhanced power factor and also led to the reduction in the thermal conductivity of $Zr_{0.25}Hf_{0.75}NiSn$-based materials. Further, Bhardwaj et al.[15] have shown HH($1-\delta$)/FH(δ) composites in the composition $Zr_{0.7}Hf_{0.3}Ni_{1+\delta}Sn$ ($0 \leq \delta \leq 0.1$), and they have observed a significant enhancement in the power factor along with reduced thermal conductivity owing to the wide range of sizes of FH inclusions and have realized a significantly improved *ZT* of ~0.96 at 773 K in $Zr_{0.7}Hf_{0.3}Ni_{1.03}Sn$. Chauhan et al.[17] also have discussed the coexistence of the HH/FH phase as well as Ni antisite defects in $ZrNi_{1+\delta}Sn$ for $0.03 < \delta < 1$, and they have observed that the maximum reduction in the lattice thermal conductivity of $ZrNi_{1+\delta}Sn$ for $0.03 \leq \delta \leq 0.05$ due to the collective scattering via Ni antisite defects and also the FH phase boundary. Furthermore, Chauhan et al.[12] have studied the effect of an excess of Ni of up to 10 atom % in ZrNiSn and observed that ultralow Ni doping results in FH precipitates as well as Ni-induced defects in the ZrNiSn-HH matrix. They have realized that carrier localization and energy filtering aid in enhancing the power factor. However, the reduction in thermal conductivity was realized due to the scattering of phonons via Ni-induced antisite defects as well as FH precipitates. Here, it may be noted that Romaka et al.[18] have not detected any FH phase up to $\delta = 0.3$ in $ZrNi_{1+\delta}Sn$ synthesized at 1073 K. Recently, Li et al.[19] have not realized the FH phase in $ZrNi_{1+\delta}Sn$ up to $\delta = 0.07$ and 0.13 synthesized at 973 and 1173 K, respectively. However, they have observed a slight increase in the lattice constant below $\delta = 0.13$ in a single HH phase and thus concluded that the excess Ni is supposed to sit at the interstitial void in the HH alloys.

In addition to the FH phase, several other competing binary phases of Zr−Sn, Ni−Sn, Ni−Zr, and ternary phases of Zr−Ni−Sn have also been predicted by Yonggang et al.[20] via theoretical calculations, which might grow as a secondary phase during the synthesis of the ZrNiSn HH compound. Chai et al.[13] have observed a small amount of Zr_5Sn_3 as the secondary phase in ZrNiSn HH. However, they have observed the ZrNiSn-HH single phase with Heusler inclusion in the composition $ZrNi_{1.1}Sn$. Guzik et al.[21] have observed the two HH phases in ZrNiSn, which were detected by high-resolution synchrotron powder X-ray diffraction (XRD). However, these were not observed in XRD and low-resolution synchrotron XRD; additionally, the impurities of Sn and ZrO were also traced. Also, they have observed the impurities of Sn and Zr_5Sn_4 in addition to two HH phases in $Hf_{0.5}Zr_{0.5}NiSn$. Li et al.[19] have done phase boundary mapping, and they also have observed some impurity phases of Sn−Zr and Ni−Sn in the ZrNiSn HH compound. The Ni_3Sn_4 phase was detected by Yang et al.[22] in ZrNiSn-HH, and they have also shown the coexistence of Ni-interstitial and Zr/Sn atomic disorders in ZrNiSn-based compound. Wang et al.[23] have detected the minority phases of Zr_5Sn_3 and $ZrNi_2Sn$ in ZrNiSn. Sauerschnig et al.[24] have performed a detailed experimental and theoretical study on the constitution of the Zr−Ni−Sn system and provided a novel thermodynamic assessment of the ternary Zr−Ni−Sn. Here, it is to be noted that careful analysis is required to understand the structural aspect of the synthesized ZrNiSn-based HH alloys. In a nutshell, it is observed that several secondary phases have earlier been detected in the synthesis of ZrNiSn-based HH alloys.

The coexistence of HH/FH/(interstitial Ni defects) works in a way that FH inclusion is metallic, which improves electronic transport, and interstitial Ni defects originate from the intermediate bands inside the electronic band gap, and in combination with the in situ formation of FH and interstitial Ni defects in HH, it significantly improves electronic transport properties. On the other hand, the miscibility gap of the HH and FH phases provides grain boundaries, and Ni interstitials contribute as point defects to scatter phonons. Collectively, all scale hierarchical phonon scattering occurs, which reduces thermal conductivity.[12] FH inclusion in the HH matrix is a well-studied technique to improve the power factor and reduce thermal conductivity.[10,12,14,15] On the other side, the doping approach is also highly preferable for reducing thermal conductivity. The atoms with different sizes and/or mass are used as dopants, which cause the strain field fluctuation and/or mass fluctuation phonon scattering. In ternary ZrNiSn, the doping of Ti and/or Hf has been widely studied to reduce κ_l.[25−28] In the way of developing Hf-free material, other dopants like Ta,[6] La,[7] Si,[29] Ge,[8,29] Pd,[25] Nb,[30] etc. have also been found effective for reducing thermal conductivity. In our recent study, we have realized isoelectronic Ge as a potential dopant at the Sn-site in ZrNiSn, the mass and size difference of Sn/Ge cause mass and strain field fluctuation, which is responsible for the scattering of phonons and thus leads to a decrease of the lattice thermal conductivity.

In the earlier works, both the approaches $Ni_{1+\delta}$ and Ge-doping have individually been seen to be effective for the enhancement of TE performance.[6−8,10,12,17] Therefore, in the present work, we have explored the TE properties of ZrNiSn employing both approaches $Ni_{1+\delta}$ and Ge-doping, simultaneously. Thus, we have synthesized $ZrNi_{1.04}Sn_{1-x}Ge_x$ (x = 0−0.04) alloys and characterized them for TE properties. As in earlier studies,[12,17,31] a low amount of Ni excess has been demonstrated to be effective; thus, we have fixed the excess of Ni at 4.0 atom %. We have checked our samples' stoichiometry and existing phases employing a laboratory-based-XRD, synchrotron XRD, field-emission scanning electron microscope (FESEM), energy-dispersive spectroscopy (EDS), and Electron Probe Micro Analyzer (EPMA). Further, the in situ-formed minor phases have been discussed. Furthermore, we have also studied the ZrNiSn-HH, $ZrNi_2Sn$-FH, $ZrNi_{1.04}Sn$, and Ge-doped $ZrNi_{1.04}Sn$, compounds with the help of theoretical calculations. The electronic band structure, density of states, and electronic transport properties were predicted for all of the alloys. In addition, the phonon band structure and the lattice thermal conductivity were also theoretically calculated. Further, mechanical properties like microhardness and fracture toughness have also been experimentally extracted to ensure that the enhanced TE performance is not at the cost of mechanical robustness.

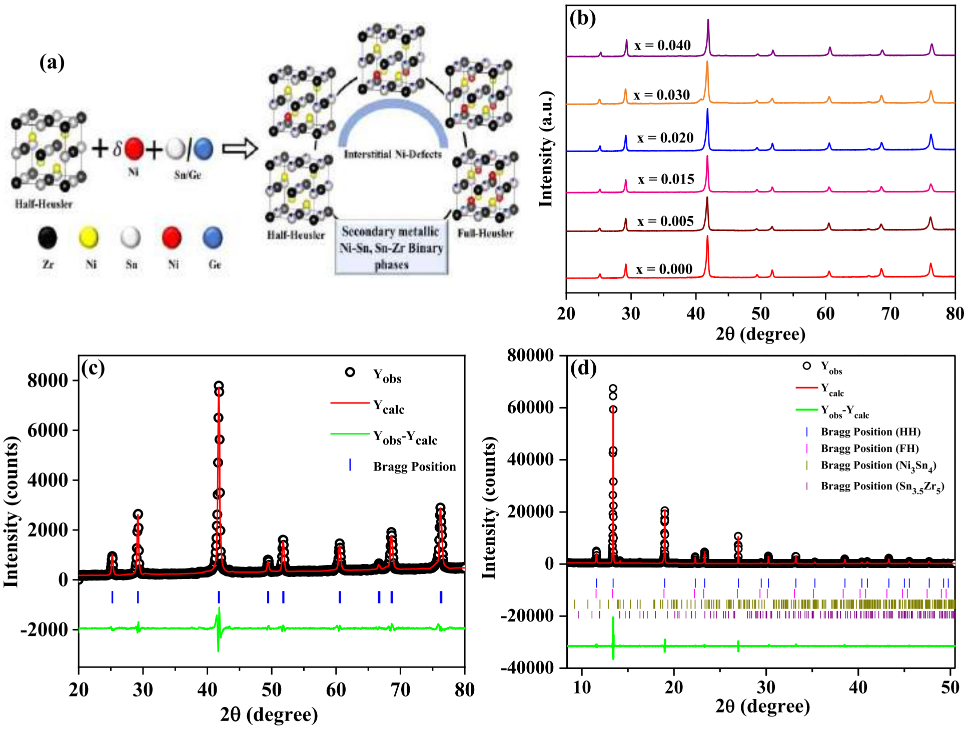

Figure 1. (a) Schematic representation of half-Heusler (HH), full-Heusler (FH), and disordered crystal structures. (b) X-ray diffraction patterns of $ZrNi_{1.04}Sn_{1-x}Ge_x$ (x = 0–0.04). (c) Rietveld refined pattern of XRD spectra of $ZrNi_{1.04}Sn$. (d) Rietveld refinement of the synchrotron XRD (SXRD) pattern of $ZrNi_{1.04}Sn_{0.98}Ge_{0.02}$.

2. COMPUTATIONAL DETAILS

The theoretical calculations on proposed systems were performed by employing density functional theory-based code Vienna Ab initio Simulation Package (VASP)[32] in which the projected augmented wave method is used for calculations of pseudo-potentials of elements. In the form of exchange and correlations functional, we adopted Perdew et al.[33,34] form of generalized gradient approximation in all sets of calculations. The use of gradient-corrected AM05 functional[35−37] in calculations predicts the precise lattice constant and hence the phonon frequency. We first optimized the cell basis vectors as well as atomic positions using conjugate gradient approximation to limit the net residual Hellman−Feynman force $\leq 1 \times 10^{-4}$ eV Å^{-1} on atomic species. Further, we have used the PHONOPY[38] code as a calculator for deriving the phonon-related properties including lattice thermal conductivity while considering the finite displacement method.

To expand plane-wave basis sets, we use a kinetic energy cutoff equal to 550 eV, and the energy convergence for all sets of computations was set to 10^{-6} eV. For exploring electronic properties, a Γ-centered 15 × 15 × 15 (4 × 4 × 4) k-points mesh was considered for unit cell (supercell) calculations. The integration of the Brillouin zone was performed by the Gaussian method with a smearing width of 0.10 eV. To prepare alloys, we have generated a 3 × 3 × 3 size supercell with the help of three atom unit cells, each of Zr, Ni, and Sn. The substitution of one Ni or Ge atom followed at the respective site gives a doping concentration of 0.037 (in fraction), which is quite close to the experimental value of 0.04. For the calculations of lattice thermal conductivity, we compress and expand the lattice by an amount of 0.02 Å from its optimized structure.

3. EXPERIMENTAL DETAILS

The samples of the composition $ZrNi_{1.04}Sn_{1-x}Ge_x$ (x = 0–0.04) have been synthesized by arc-melting, followed by spark plasma sintering (SPS). The high-purity elements Zr, Ni, Sn, and Ge were taken in the stoichiometric proportion and then melted employing an arc-melting unit (MAM-1) under the argon atmosphere. The arc-melted ingots were flipped and remelted several times to ensure homogeneity and then consolidated employing SPS (Dr. Sinter, 725) at 1473 K under ∼50 MPa. The density of all the synthesized samples was measured by utilizing the Archimedes principle. The phase purity of the synthesized samples was checked using the X-ray diffraction technique (XRD; Rigaku Miniflex II), and synchrotron X-ray diffraction measurements were performed on an Angle Dispersive X-ray diffraction beamline (BL-12) on Indus-2 synchrotron source, Indore.[39] This beamline consists of a Si 111-based double crystal Monochromator. Monochromatic energy of 17.413 keV was used to record XRD data on a 6-circle diffractometer (Huber 5020) with a Dectris make mythen detector. Further, the surface morphology and elemental proportion were determined by field-emission scanning electron microscopy (FESEM; Carl-Zeiss Merlin Compact and Zeiss (Supra 40VP)) and EDS from Oxford Instruments. The Electron Probe Micro Analyzer (EPMA: JXA-8230; JEOL) was further used to investigate elemental composition.

The thermal diffusivity of the samples was determined employing a laser flash analyzer (LFA; Linseis 1000) and Seebeck coefficient along with resistivity measured using a ULVAC, ZEM 3. Specific heat was determined utilizing a differential scanning calorimeter (DSC-NETZSCH, 404 F3). The room temperature carrier concentration and mobility were determined using the Hall effect measurement system (HEMS, Nanomagnetics). The schematic crystal structure was visualized using VESTA software.

To determine the microhardness and fracture toughness of all well-polished samples, Future Tech equipment (FM-e7) was used in conjunction with a square diamond pyramidal indenter (136°), and the indentation load was fixed at 4.9 N with a 10 s dwell period. The length of the produced cracks due to the indentation was measured using an in-built microscope with a micrometer scale in the Vickers microhardness system to compute the fracture toughness of the materials. We also estimated the standard deviation of the mechanical properties after repeating the measurement four times.

4. RESULTS AND DISCUSSION

The schematic representation of half-Heusler (HH), full-Heusler (FH), and disordered crystal structures is displayed in Figure 1a. The X-ray diffraction (XRD) patterns of all of the synthesized $ZrNi_{1.04}Sn_{1-x}Ge_x$ (x = 0−0.04) samples are shown in Figure 1b. All of the observed peaks suggest the formation of the HH phase. To confirm the phase purity, the XRD patterns were profile fitted for the HH phase employing the Rietveld refinement method using the FullProf Suite package. The fitting parameters are shown in Table 1, and the fitting of $ZrNi_{1.04}Sn$ is given in Figure 1c. From Table 1, it is clear that the variation in the lattice parameter is very small and does not follow any pattern with increasing Ge-content. This kind of behavior has been realized due to secondary phases.[40] Here, it may be noted that in Ni excess MNiSn (M = Hf, Ti, Zr)-based samples, the FH phase has been observed previously.[10,12,14,15,17] Further, Yonggong et al.[20] have predicted some secondary phases of Ni−Sn, Zr−Sn, etc. Sometimes, these FH and minor secondary phases are not detected in laboratory-source-XRD and thus need better resolution.

Table 1. Lattice Parameter (a), Goodness-of-Fit Parameter (χ^2) of Rietveld Refinement, Room Temperature Carrier Concentration (n_H), and mobility (μ_H) of $ZrNi_{1.04}Sn_{1-x}Ge_x$ (x = 0−0.04)

	rietveld refinement		hall measurement	
x	a (Å)	χ^2	n_H (10^{19} cm^{-3})	μ_H (cm^2 v^{-1} s^{-1})
0	6.1158(3)	2.880	5.05	17.86
0.005	6.1186(4)	3.731	6.98	14.81
0.015	6.1134(3)	2.448	4.59	18.61
0.02	6.118(2)	4.631	6.97	15.40
0.03	6.1087(2)	4.723	7.08	14.64
0.04	6.1133(1)	3.193	11.6	12.72

For the compositional analysis of the existing secondary phases that were hard to detect in the laboratory-source-XRD due to its detection limit, synchrotron XRD (SXRD) characterization was performed on a representative sample $ZrNi_{1.04}Sn_{0.98}Ge_{0.02}$, and the observed spectra were profile fitted using the Rietveld refinement method, as shown in Figure 1d. The parameters of refinement are given in Table 2. The results suggest the formation of the HH phase as the primary matrix and the in situ growth of secondary phases of FH, $Sn_{3.5}Zr_5$, and Ni_3Sn_4. The FH has previously been observed in MNiSn-based[23,41] and $MNi_{1+\delta}Sn$-based[10,12,14,15,17] materials. However, the binary phases of Ni−Sn and Zr−Sn have earlier been observed in MNiSn.[13,19,21−23]

The surface morphology of the samples $ZrNi_{1.04}Sn$ along with $ZrNi_{1.04}Sn_{0.98}Ge_{0.02}$ have been investigated employing FESEM. The FESEM micrograph of the fractured surface of $ZrNi_{1.04}Sn$ is shown in Figure 2a, which suggests the formation of a highly dense material. Furthermore, Figure 2b shows the FESEM micrograph of the polished surface of $ZrNi_{1.04}Sn$, which also confirms the tight compaction of the grains and exhibits an average grain size closely in the range of 10−40 nm. Similarly, the $ZrNi_{1.04}Sn_{0.98}Ge_{0.02}$ sample was also studied, and the FESEM micrograph of fractured (Figure 2c) and polished surface (Figure 2d) supports the close packing in the material.

The elemental composition was studied using EDS analysis for the representative sample $ZrNi_{1.04}Sn_{0.98}Ge_{0.02}$, and the observed results are given in Figure 3. Figure 3b exhibits the overall EDS analysis of Figure 3a, which confirms the presence of all of the constituent elements in the sample, and shows the elemental proposition close to the HH phase with a small amount of Ni excess, which supports the inclusion of additionally added Ni in ZrNiSn. Further, the EDS analysis of different regions marked as 1, 2, and 3 is shown in Figure 3c−e. The regions marked as 1 and 2 show the stoichiometry close to FH alloys and the Zr−Sn phase of $Sn_{3.5}Zr_5$, respectively. The region marked as 3 is the HH alloy with some considerable excess Ni. As discussed above, in addition to the HH, FH, and Sn−Zr phase ($Sn_{3.5}Zr_5$), the Ni−Sn (Ni_3Sn_4) phase was also observed in SXRD, and a similar kind of Ni−Sn (Ni_3Sn_4) phase was observed in Figure 3f−g.

Furthermore, we have performed the EPMA measurement shown in Figure 4 on our sample $ZrNi_{1.04}Sn_{0.97}Ge_{0.03}$. In Figure 4, the gray contrast shows the HH composition, whereas the dark gray contrast reflects the FH phase. Further, the bright gray contrast exhibits the Sn−Zr ($Sn_{3.5}Zr_5$) phase with a slight amount of Ni. This small amount of Ni in the Sn−Zr phase might be the result of grain boundaries, similar to the small amount of Zr that has been observed previously in the Ni_3Sn_4 secondary phase grown in $Zr_9Ni_7Sn_8$.[42] From the structural analysis, which includes XRD, SXRD, FESEM along with EDS, and EPMA, it is clear that the in situ formation of the FH, Sn−Zr, and Ni−Sn phases appeared when an excess amount of Ni was added, and the secondary phases have also been observed previously in MNiSn-based materials and also predicted theoretically.[12−15,17,20−23]

The calculated electronic band structure and projected density of states (PDOS) of ZrNiSn, $ZrNi_2Sn$, $ZrNi_{1.04}Sn$, and Ge-doped $ZrNi_{1.04}Sn$ are given in Figure 5. The band structure of pristine ZrNiSn, as shown in Figure 5a, exhibits an indirect energy band gap of 0.55 eV.[20] Its valence band maximum (VBM) lies at the Γ point, while conduction band minimum (CBM) lies at the X point of the Brillouin zone. To enhance our understanding of the origin of these frontier states, we next calculated its projected density of states (PDOS), illustrated in Figure 5b, which confirms that Zr-4d orbitals are majorly dominant at the edge of the valence band, while the conduction band edge is formed by mixed states of mainly Zr-4d and Ni-3d orbitals. However, in the energy range of −0.3 to −0.5 eV, Zr-4p, Ni-4p, and Ni-3d orbitals strongly hybridize and are responsible for states in the vicinity of the VBM. Before studying our defective system of excess Ni in ZrNiSn, we attempted to understand the electronic properties of the $ZrNi_2Sn$-FH compound. Our calculated band structure and

Table 2. Rietveld Refined Parameters of SXRD of $ZrNi_{1.04}Sn_{0.98}Ge_{0.02}$

				ZrNiSn (cubic)	$ZrNi_2Sn$ (cubic)	Ni_3Sn_4 (monoclinic)				$Sn_{3.5}Zr_5$ (hexagonal)	
R_p	R_{wp}	R_e	χ^2	a (Å)	a (Å)	a (Å)	b (Å)	c (Å)	(°)	$a = b$ (Å)	c (Å)
13.5	14.4	6.81	4.49	6.1053(1)	6.1327(3)	12.2273(1)	4.0543(1)	5.1927(1)	104.895	8.505(2)	5.804(2)

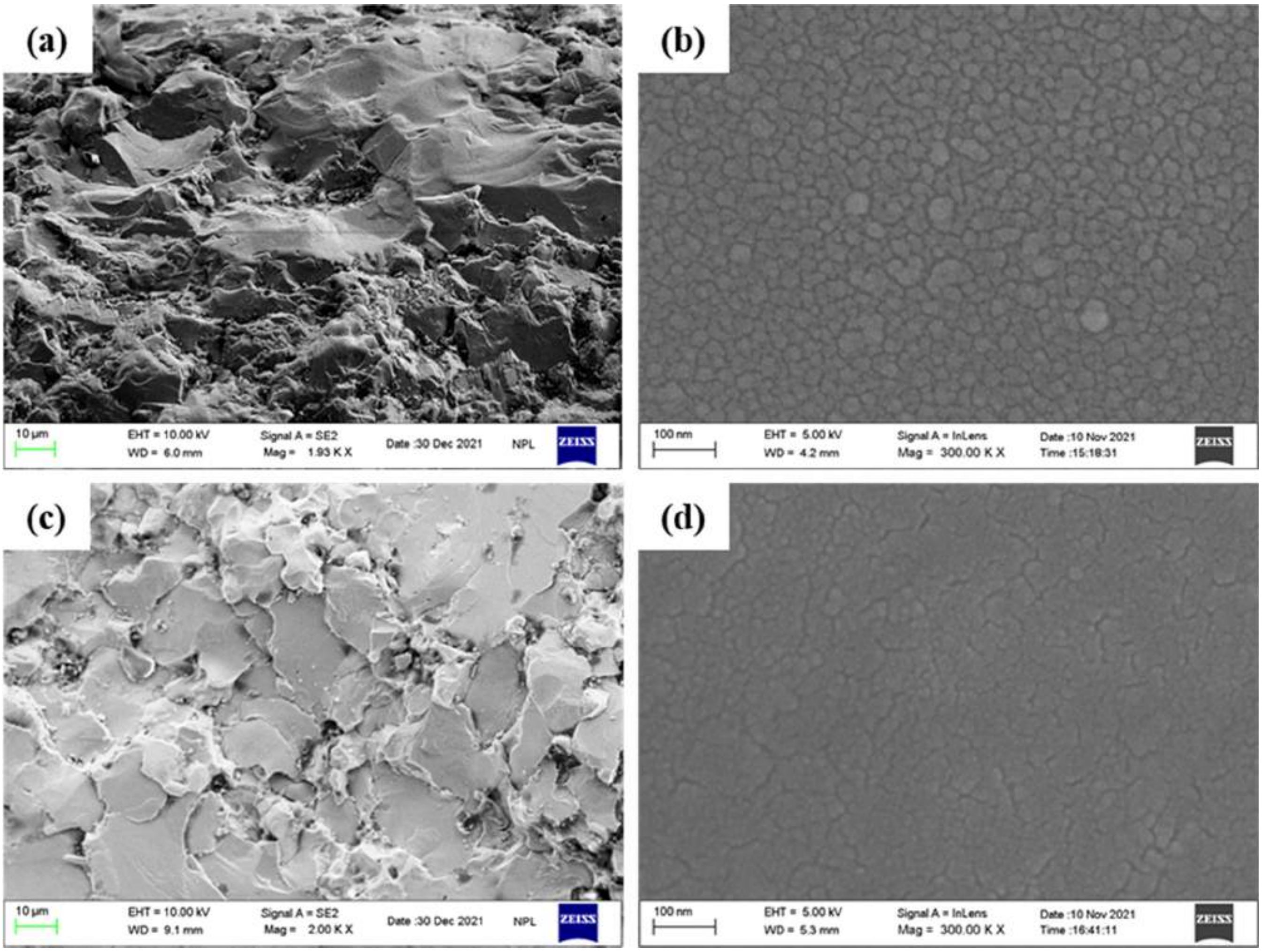

Figure 2. FESEM images of (a) fractured and (b) polished surfaces of $ZrNi_{1.04}Sn$ and (c) fractured and (d) polished surfaces of $ZrNi_{1.04}Sn_{0.98}Ge_{0.02}$.

PDOS of $ZrNi_2Sn$ are given in Figure 5c,d, respectively. From Figure 5c,d, it is clear that $ZrNi_2Sn$ is metallic in nature, as also predicted previously.[43] It may occur due to the extra Ni atom introduced to completely fill the 4d (3/4 3/4 3/4) site, which introduces electronic states in the energy gap to make the transition of semiconductor ZrNiSn to metallic $ZrNi_2Sn$. Further, the electronic structure of $ZrNi_{1.04}Sn$ was studied. To capture the electronic properties of $ZrNi_{1.04}Sn$, we calculated its band structure and PDOS, as shown in Figure 5e,f, respectively. From Figure 5e, it is clear that incorporating Ni into ZrNiSn introduces new energy bands into forbidden energy regions that may be called intermediate bands (IBs). These IBs lie above (below) the VBM (CBM). This opens a new era of its application in optoelectronic devices because such IBs may enhance the population of optical transitions. The IBs mainly originated from excess Ni-3d orbitals with a minor contribution of Zr-4d and Sn-5p orbitals (see Figure 5f). A more detailed investigation about IBs is needed but is out of the theme and scope of the present paper. Furthermore, it may deviate from the central theme of the work. Therefore, we skipped its further investigations.

Greater electron mobility is expected by the transition from the lower valence band to IB to the conduction band, and hence improved electron mobility is expected. The incorporation of excess Ni enhanced the contribution of Sn-5p orbitals at the valence band edge in comparison to appearing in ZrNiSn; however, no drastic change was predicted at conduction band edge states. Further, the inclusion of Ge into the Ni-excess ZrNiSn system retains the electronic structure similar to that predicted for $ZrNi_{1.04}Sn$, as illustrated in Figure 5g,h. Looking at the band structure of the Ni-excess and Ge-doped system, it is clear that the maxima and minima of frontier states mainly lie at the X point of the Brillouin zone; thus, it would be interesting to calculate the effective mass for electrons and holes. We have calculated the effective mass of electrons and holes while moving along the $L-\Gamma$ and $X-\Gamma$ directions. Our calculated value of the effective mass of the electrons (holes) of pristine ZrNiSn-HH comes to 0.65 (0.90) m_e. In the case of Ni-excess and Ge-doping, the effective mass of the electrons (holes) is lower (higher) and is equal to 0.48 (4.30) m_e and 0.50 (3.93) m_e, respectively, than that of pristine ZrNiSn-HH. The reduction in the electron effective mass indicates that it is expected that the electrical conductivity increases for Ni-excess and Ge-doped systems.

To further deepen our understanding of the TE performance of the alloys, we next concentrate on the calculations of electronic transport properties. The electrical conductivity scaled by relaxation time (σ/τ), Seebeck coefficient, and power factor scaled by relaxation time ($S^2\sigma/\tau$) of ZrNiSn, $ZrNi_{1.04}Sn$, and Ge-doped $ZrNi_{1.04}Sn$ at different temperatures are shown in Figure 6. And it is clear from Figure 6a−c that σ/τ increases with increasing temperature in the vicinity of the Fermi level.

https://doi.org/10.1021/acsami.2c03065

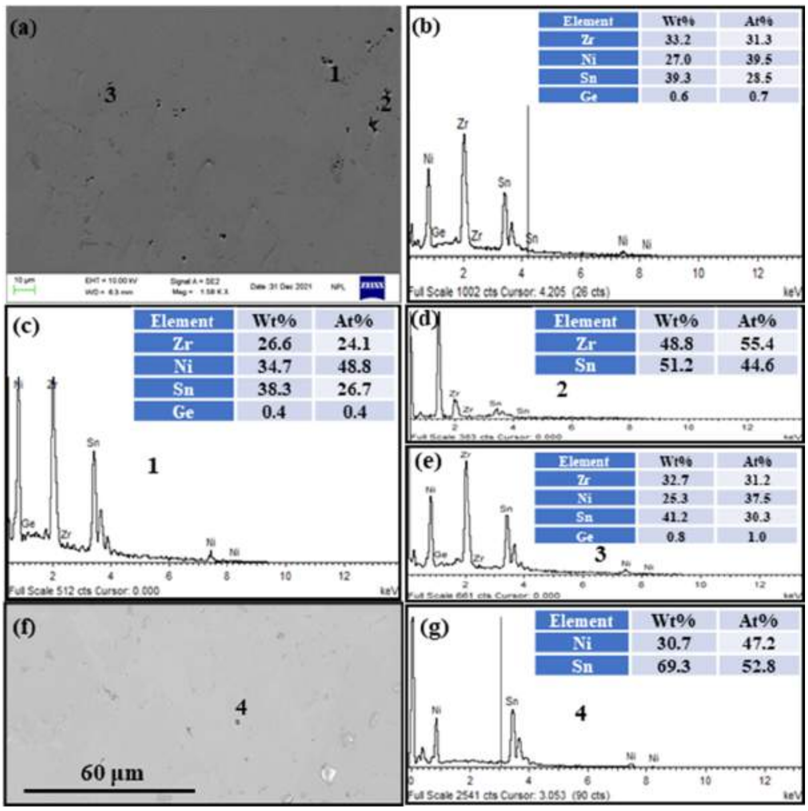

(b)

Element	Wt%	At%
Zr	33.2	31.3
Ni	27.0	39.5
Sn	39.3	28.5
Ge	0.6	0.7

(c)

Element	Wt%	At%
Zr	26.6	24.1
Ni	34.7	48.8
Sn	38.3	26.7
Ge	0.4	0.4

(d)

Element	Wt%	At%
Zr	48.8	55.4
Sn	51.2	44.6

(e)

Element	Wt%	At%
Zr	32.7	31.2
Ni	25.3	37.5
Sn	41.2	30.3
Ge	0.8	1.0

(g)

Element	Wt%	At%
Ni	30.7	47.2
Sn	69.3	52.8

Figure 3. EDS analysis of $ZrNi_{1.04}Sn_{0.98}Ge_{0.02}$. (a) FESEM image. (b) EDS analysis of the image shown in (a). (c–e) EDS analysis of the marked regions 1, 2, and 3. (f) FESEM image. (g) EDS analysis of marked region 4.

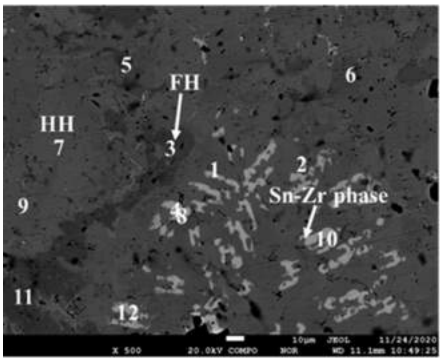

Region	Zr	Ni	Sn	Ge
	Atomic ratio			
1	31.9233	35.893	31.8025	0.3812
2	30.6101	36.736	32.46	0.194
3	24.5151	48.439	26.4831	0.5628
4	51.7515	12.2025	33.1563	2.8896
5	28.5009	37.024	33.3584	1.1167
6	29.1321	36.5488	33.2162	1.103
7	28.3319	37.3727	33.2662	1.0293
8	53.2474	8.5058	35.6162	2.6306
9	29.0618	36.4567	33.3554	1.1261
10	50.5923	8.8199	35.5685	5.0194
11	22.4727	47.6553	28.9036	0.9685
12	50.8746	8.9554	37.2875	2.8825

Figure 4. Electron Probe Micro Analyzer (EPMA) image and the atomic ratio of constituent elements of $ZrNi_{1.04}Sn_{0.97}Ge_{0.03}$.

Further, the enhancement in σ/τ is realized in $ZrNi_{1.04}Sn$ compared to that of ZrNiSn in the entire temperature in the vicinity of the Fermi level, and this enhancement may be attributed to the appearance of intermediate bands in the energy band gap owing to the excess Ni. Furthermore, the Seebeck coefficient (S) shown in Figure 6d–f decreases when Ni is added in ZrNiSn, which may be due to the reduction in the effective mass calculated above. In conjunction, σ/τ and S exhibit increasing $S^2\sigma/\tau$ (see Figure 6g–i) with increasing temperature in the vicinity of the Fermi energy level, and this behavior is consistent with the experimental observations of the power factor (will be discussed in the following section). However, $ZrNi_{1.04}Sn$ exhibits higher $S^2\sigma/\tau$ than that of ZrNiSn at all temperatures, which may be due to the emergence of IBs between the valence and conduction band edges, which led to the enhanced population of transitions, and thus a large electrical conductivity is expected. Further, $ZrNi_{1.04}Sn$ and Ge-doped $ZrNi_{1.04}Sn$ exhibit more or less similar electronic transport properties at all temperatures, which is analogous to their comparable band structure (Figure 5).

To realize this experimentally, the synthesized samples were characterized for TE properties, and the temperature-dependent electronic transport properties of all of the synthesized samples $ZrNi_{1.04}Sn_{1-x}Ge_x$ ($x = 0–0.04$) are shown in Figure 7. The electrical conductivity is given in Figure 7a, which suggests the semiconducting behavior of all of the synthesized samples as the electrical conductivity increases with increasing temperature. We have observed that the σ of $ZrNi_{1.04}Sn$ is higher than that of the pristine ZrNiSn[8] system in the entire temperature range, which is in agreement with the earlier reports.[14,44] Further, with Ge-doping, σ at RT does not change significantly up to 1.5 atom %, beyond which a noticeable increase has been observed. At high temperatures, all of the Ge-doped samples exhibited enhanced σ compared to their

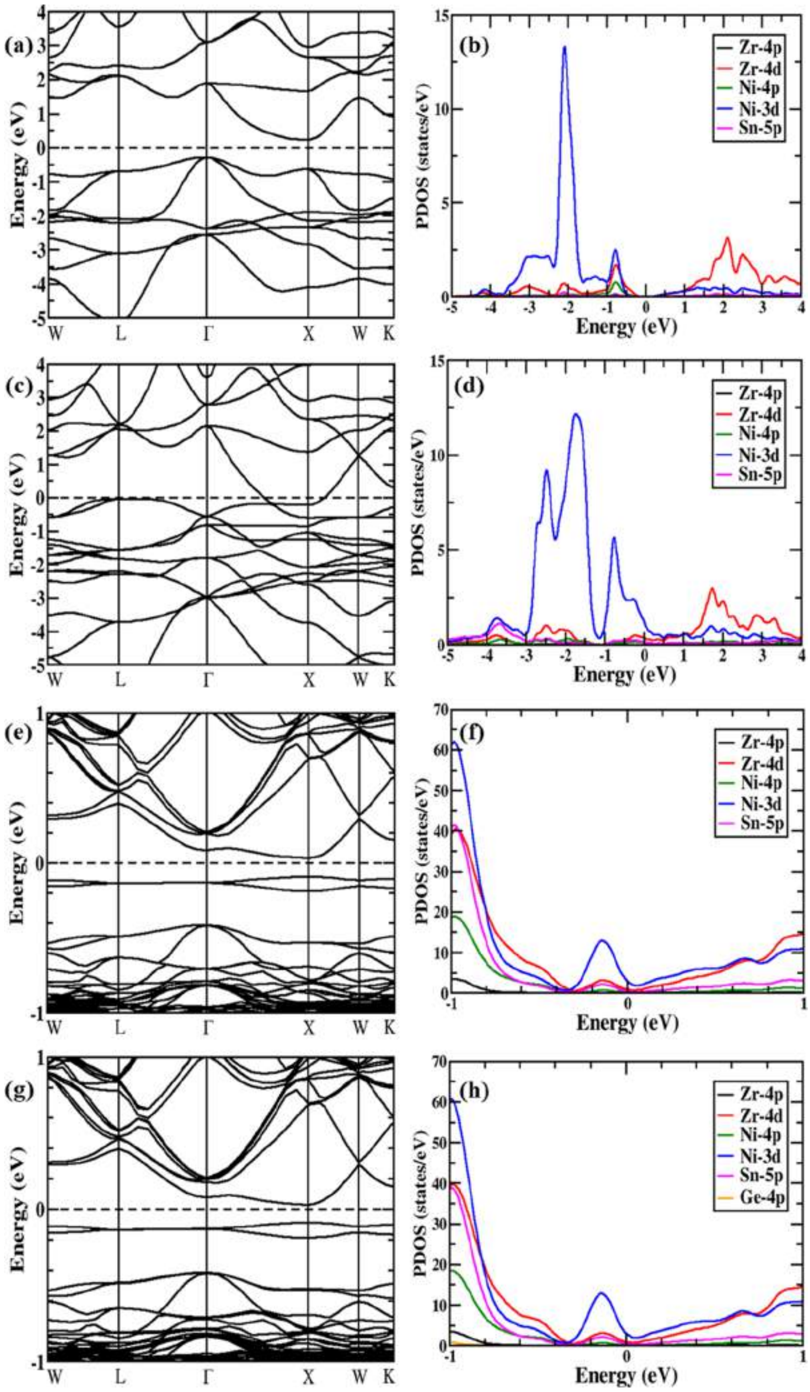

Figure 5. Calculated electronic band structures and projected density of states (PDOS) of (a, b) ZrNiSn, (c, d) $ZrNi_2Sn$, (e, f) $ZrNi_{1.04}Sn$, and (g, h) Ge-doped $ZrNi_{1.04}Sn$.

pristine counterpart $ZrNi_{1.04}Sn$, and similar observations have been made previously with Ge-doping in ZrNiSn.[8]

Figure 7b exhibits the temperature-dependent Seebeck coefficient of all of the synthesized samples; the negative sign suggests that the electrons are dominant in electrical transport. It is clear from Figure 7b that the S of $ZrNi_{1.04}Sn$ is lower than that of ZrNiSn,[8] which is similar to previous reports.[14,44] The Seebeck coefficient at RT was found to be lower in all of the Ge-doped compositions as compared to that of $ZrNi_{1.04}Sn$, and this behavior is in agreement with the previous study of Ge-doping in ZrNiSn.[8]

To analyze the electronic transport properties, we have measured room temperature Hall carrier concentration (n_H) and mobility (μ_H) (given in Table 1). Both the n_H and μ_H of $ZrNi_{1.04}Sn$ are higher than that of ZrNiSn.[8] The realized appearance of intermediate bands in the electronic band structure of $ZrNi_{1.04}Sn$ (Figure 5e) might be attributed to this enhancement. Furthermore, it can be realized that Ge-doped samples exhibit improved n_H and decreased μ_H relative to its pristine counterpart $ZrNi_{1.04}Sn$, except for $ZrNi_{1.04}Sn_{0.985}Ge_{0.015}$. However, the electronic band structure and PDOS of $ZrNi_{1.04}Sn$ and Ge-doped $ZrNi_{1.04}Sn$, shown in Figure 5e–f, are more or less similar and do not suggest any

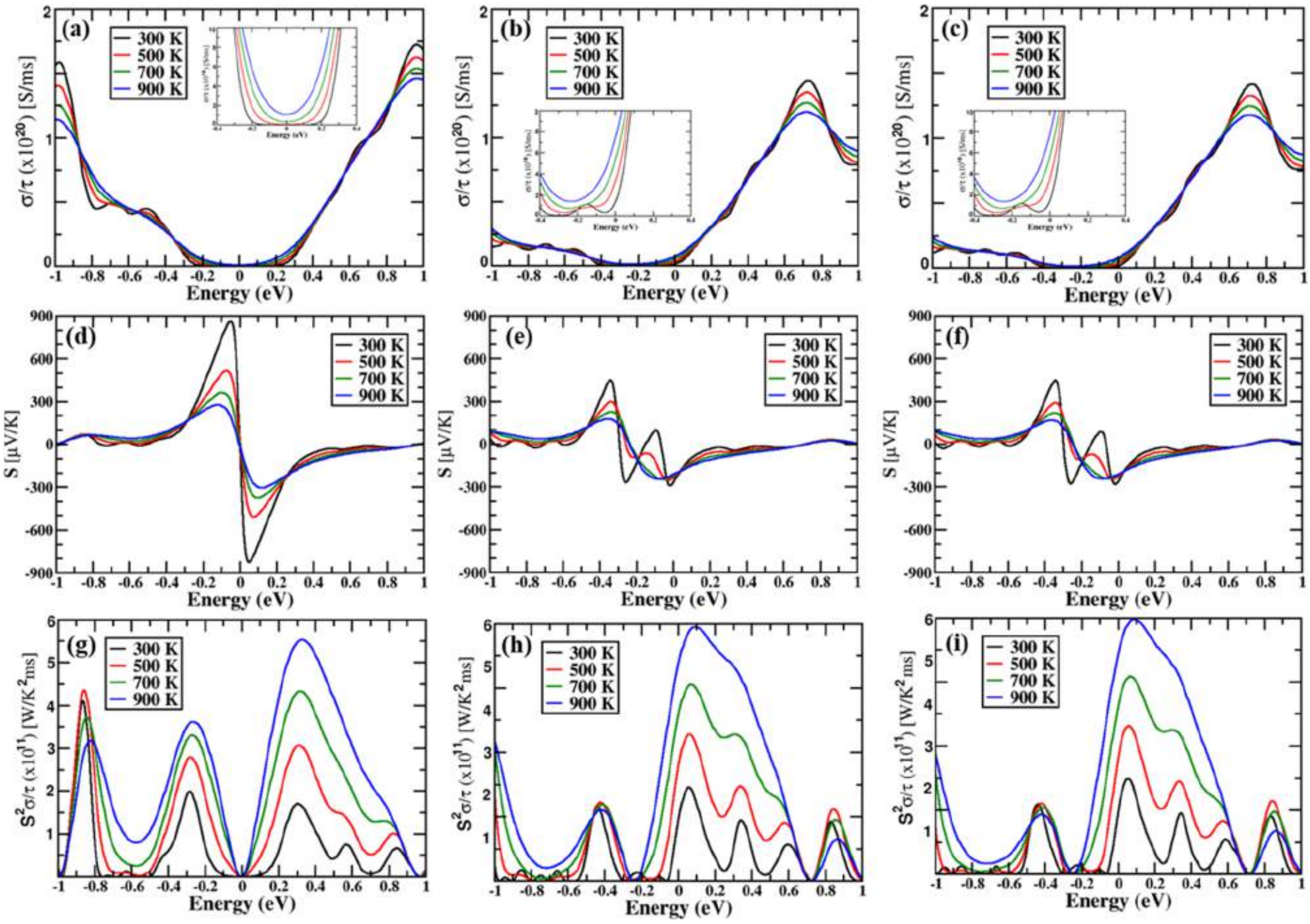

Figure 6. Calculated electronic transport properties of ZrNiSn, $ZrNi_{1.04}Sn$, and Ge-doped $ZrNi_{1.04}Sn$, left to right: (a−c) σ/τ (inset: magnified from −0.4 to 0.4 eV), (d−f) Seebeck coefficient, and (g−i) power factor, respectively.

significant change. Here, it may also be noted that in the previous observation, it has been realized that n_H with Ge-doping in ZrNiSn does not change significantly.[8] However, in the present study, Ge-doping in $ZrNi_{1.04}Sn$ affects the n_H. This anomalous behavior may be attributed to the in situ formation of secondary phases, as discussed above; further, to understand the underlying physics, we have applied the single parabolic band (SPB) model.[45,46]

The single parabolic band (SPB) model[45,46] was applied at room temperature. The Pisarenko plot is plotted using the equations based on the SPB model considering scattering by acoustic phonons[45,46]

$$S = \frac{k_B}{e}\left(\frac{2F_1(\eta)}{F_0(\eta)} - \eta\right)$$

Chemical carrier concentration, $n = 4\pi\left(\frac{2m^* k_B T}{h^2}\right)^{3/2} F_{1/2}(\eta)$

Hall carrier concentration, $n_H = \frac{n}{r_H}$, where the Hall factor, $r_H = \frac{3}{2}F_{1/2}(\eta)\frac{F_{-1/2}(\eta)}{2F_0^2(\eta)}$

where k_B is the Boltzmann constant, e is the electronic charge, Fermi integral, $F_j(\eta) = \int_0^\infty \frac{\epsilon^j \, d\epsilon}{1 + \text{Exp}(\epsilon - \eta)}$, m^* is the density of states effective mass, T is the temperature, and h is Planck's constant. Figure 7c shows the calculated Pisarenko plot taking the average effective mass $m^* = 2.49$ m_e and scattering by acoustic phonons. Here, the calculated m^* of all of the samples is in the range 2.18−2.82 m_e. The variation in m^* may be attributed to the formation of secondary phases as the electronic band structure (see Figure 5e−h) does not change with Ge-doping. Therefore, various factors like structural irregularities (in situ secondary phase formation), which cause transport irregularities, scattering mechanism, band nonparabolicity, etc., might play a role in this variation of m^*.[45,47,48] Further, to clarify the nonmonotonous variation of μ_H, it is plotted with n_H in Figure 7d and also the calculated μ_H from the SPB model[45,46] using the formula, assuming scattering by acoustic phonons and taking the average effective mass $m^* = 2.49$ m_e and average $\mu_0 = 20.34$ $cm^2 V^{-1} s^{-1}$. Here, the calculated μ_0 for each sample using experimental Hall mobility lies in the range 18.16−23.59 $cm^2 V^{-1} s^{-1}$. As seen in Figure 7d, the experimentally observed μ_H is closely related to the predicted results with some deviation. This deviation might be due to the various factors involved, like structural irregularities as observed in the form of secondary phases, which cause the transport irregularities, scattering mechanism, variation in effective mass, band nonparabolicity, etc.[27,45,48,49]

The temperature-dependent power factor of all of the synthesized samples is shown in Figure 7e. It is clear from Figure 7e that the PF of the $ZrNi_{1.04}Sn$ sample is higher than that of the pure ZrNiSn.[8] Further, with simultaneous optimization of electrical conductivity and Seebeck coefficient, we have achieved the maximum α of ~4.24×10^{-3} $Wm^{-1} K^{-2}$

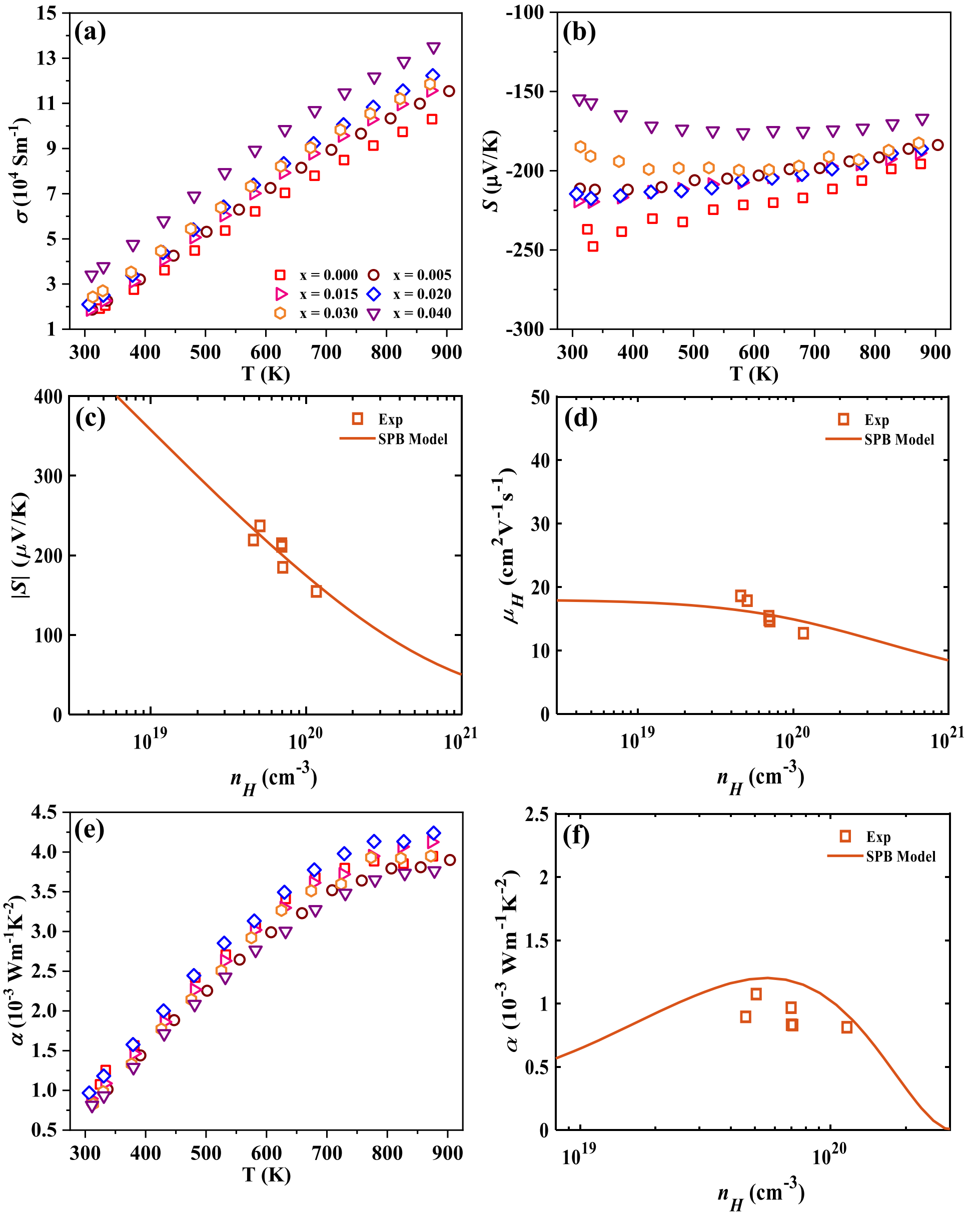

Figure 7. Temperature-dependent experimental (a) electrical conductivity and (b) Seebeck coefficient; (c) Pisarenko plot; (d) Hall mobility prediction based on the single parabolic band (SPB) model at RT; (e) power factor; and (f) power factor prediction based on the SPB model at RT of $ZrNi_{1.04}Sn_{1-x}Ge_x$ (x = 0−0.04).

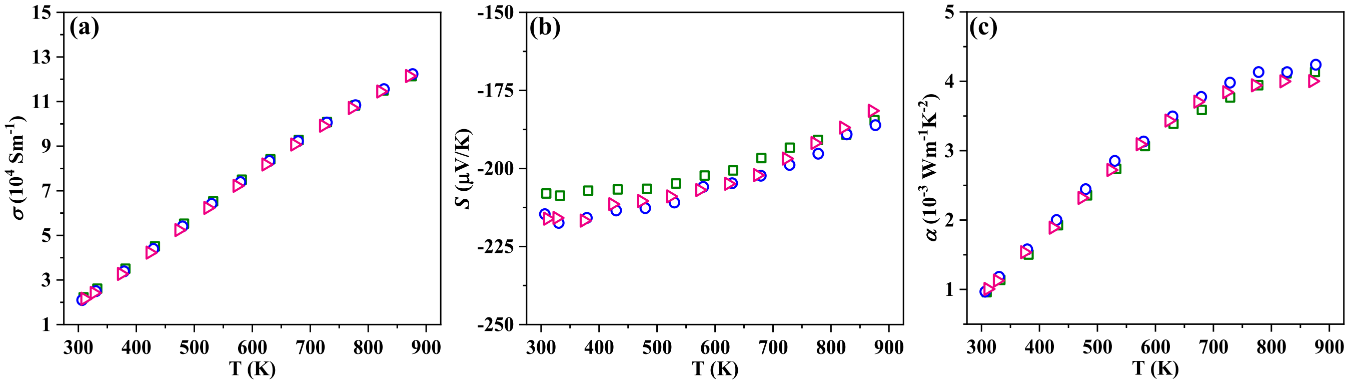

Figure 8. Repeatability measurements of (a) electrical conductivity, (b) Seebeck coefficient, and (c) power factor of $ZrNi_{1.04}Sn_{0.98}Ge_{0.02}$.

https://doi.org/10.1021/acsami.2c03065

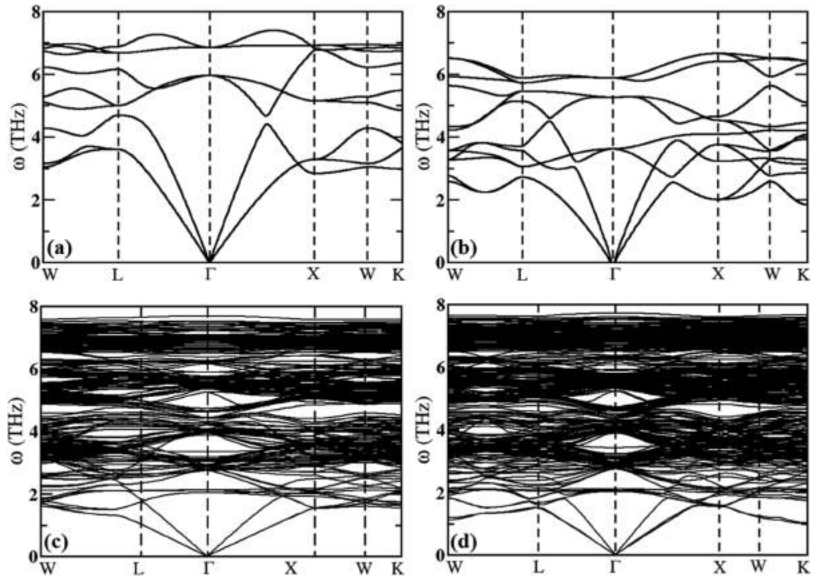

Figure 9. Phonon band structures of (a) ZrNiSn, (b) $ZrNi_2Sn$, (c) $ZrNi_{1.04}Sn$, and (d) Ge-doped $ZrNi_{1.04}Sn$.

at ∼873 K in $ZrNi_{1.04}Sn_{0.98}Ge_{0.02}$. Figure 7f exhibits the experimental power factor at RT plotted against n_H and compared with the power factor calculated by the SPB model[45,46] taking an average effective mass of 2.49 m_e and an average μ_0 of 20.34 $cm^2\ V^{-1}\ s^{-1}$ and considering scattering by acoustic phonons. As seen in Figure 7f, the Hall carrier concentration is in the optimum range, and there is still scope for improvement of the power factor as predicted by a slightly higher α by the SPB model.

Further, to check the stability of the material, we have repeated the measurements of the temperature-dependent electronic transport properties of the same sample $ZrNi_{1.04}Sn_{0.98}Ge_{0.02}$ three times, which is given in Figure 8. From Figure 8, it is clear that the observed results are consistent in each repeated measurement cycle, which suggests that the material is thermally stable.

Now, to understand the thermal transport behavior and dynamical stability, we have performed the phonon calculations of the ZrNiSn-HH, $ZrNi_2Sn$-FH, $ZrNi_{1.04}Sn$, and Ge-doped-$ZrNi_{1.04}Sn$ system. The phonon dispersion curves along the high symmetry path $W-L-\Gamma-X-W-K$ in the Brillouin zone are shown in Figure 9. From Figure 9a, it is clear that the pristine ZrNiSn system shows positive phonon frequencies in a different direction of the BZ, confirming the absence of soft modes or imaginary frequencies, which indicates that the ZrNiSn system is stable and is consistent with the other reports.[3,17,50] The phonon dispersion curve of $ZrNi_2Sn$-FH is also shown in Figure 9b, which indicates its stability. Our investigation demonstrates that there are three acoustical and six optical phonon branches in the case of ZrNiSn-HH; however, for $ZrNi_2Sn$-FH the three acoustic and nine optical branches appear. Looking at the phonon band structure of both ZrNiSn and $ZrNi_2Sn$, it is clear that the transverse acoustic as well as transverse optical modes are degenerate in the direction $L-\Gamma-X$. Along the paths $L-W$ and $X-W-X$, the degeneracy of transverse modes breaks and splitting in modes occur as clearly can be seen in both acoustic as well as optical branches. A small frequency gap is present between the acoustic and optical branches of ZrNiSn; however, this gap closes in the case of $ZrNi_2Sn$, and another separation in frequency appears in the upper and lower three optical modes. A similar type of behavior was realized in the previous study.[17] Furthermore, the incorporation of a small amount of Ni and Ge into the ZrNiSn system introduces lattice distortion, which may deviate its phonon stability. To check it, we also carried out phonon calculations of $ZrNi_{1.04}Sn$ and Ge-doped $ZrNi_{1.04}Sn$, as illustrated in Figure 9c,d, respectively. From Figure 9c–d, it is clear that no negative phonon frequency modes appear in our calculated phonon band structure, which shows that $ZrNi_{1.04}Sn$ and Ge-doped $ZrNi_{1.04}Sn$ systems are phonically stable. Since a large cell is used to calculate the phonon dispersion of $ZrNi_{1.04}Sn$ and Ge-doped $ZrNi_{1.04}Sn$, a large number of bands were obtained, and it is difficult to identify the characteristics of these bands. However, it can be observed that the degeneracy of transverse acoustic modes is maintained along the path $L-\Gamma-X$ in the phonon dispersion of $ZrNi_{1.04}Sn$ as observed in ZrNiSn-HH and $ZrNi_2Sn$-FH compounds. However, in the Ge-doped $ZrNi_{1.04}Sn$, the degeneracy of transverse acoustic modes seems to be broken along the path $L-\Gamma-X$, which might be due to the introduced imperfection via the mass difference of Ge and Sn-atom.

For pristine ZrNiSn-HH, formation energy can be computed by subtracting its total energy from the total energy of constituent atoms. Our calculated formation energy of ZrNiSn-HH is −2.13 eV/f.u., which agrees with earlier calculations.[17] The negative value of formation energy indicates that the system follows an exothermic chemical reaction while growing the sample. Further to understand the enthalpy of formation (ΔH_f) of alloys,[24] we used the following equation

$$\Delta H_f = \frac{1}{(k+l+m+n)}[E(Zr_kNi_lSn_mGe_n) - k\left(\frac{E(Zr)}{p}\right) - l\left(\frac{E(Ni)}{q}\right) - m\left(\frac{E(Sn)}{r}\right) - n\left(\frac{E(Ge)}{s}\right)]$$

where $E(Zr_kNi_lSn_mGe_n)$, $\left(\frac{E(Zr)}{p}\right)$, $\left(\frac{E(Ni)}{q}\right)$,$\left(\frac{E(Sn)}{r}\right)$, and $\left(\frac{E(Ge)}{s}\right)$ are the total energies of systems, while k, l, m, and n are the total number of atoms of Zr, Ni, Sn, and Ge in the supercell used. The p, q, r, and s denote the Zr, Ni, Sn, and Ge atoms in defective cells. In the case of Ni excess ZrNiSn and Ge-doped $ZrNi_{1.04}Sn$, the formation of the composition following an exothermic chemical reaction with negative values of ΔH_f of −0.697 and −0.701 meV, respectively. The ΔH_f for Ni excess ZrNiSn is greater than Ge-doped $ZrNi_{1.04}Sn$, which indicates that the excess of Ni demands smaller energy for the formation of compound in comparison to Ge-doping into $ZrNi_{1.04}Sn$. However, the energy difference between them is of a small order of meV. One of the reasons for changes in the followed chemical reaction can be understood by the energy differences between HH and FH compounds. We have predicted that the energy difference between ZrNiSn-HH and $ZrNi_2Sn$-FH compounds is equal to 0.29 eV/atom. Our calculated ΔH_f may act as a representative and can provide a trend of the followed chemical reaction for the growth of compounds. However, ΔH_f further depends on several parameters like Ni or Ge nearest neighboring site, the use exchange−correlation functional for computation, etc.

Furthermore, we have extended our calculation to calculate the lattice thermal conductivity of $ZrNi_{1.04}Sn$ and Ge-doped $ZrNi_{1.04}Sn$, as shown in Figure 10. It is observed that the lattice thermal conductivity of both compounds decreases with temperature. And it is predicted that Ge-doping in $ZrNi_{1.04}Sn$ reduces lattice thermal conductivity throughout the temperature range.

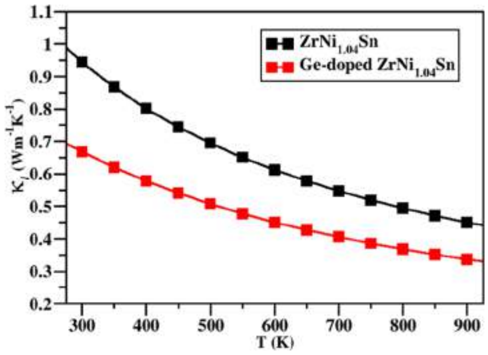

Figure 10. Temperature-dependent calculated lattice thermal conductivity of $ZrNi_{1.04}Sn$ and Ge-doped $ZrNi_{1.04}Sn$.

Next, the experimental thermal conductivity was calculated by employing the relation $\kappa = D\rho C_p$, where D is the measured thermal diffusivity, C_p is the specific heat, and ρ represents room temperature density. The temperature-dependent thermal conductivity of all of the synthesized samples is shown in Figure 11a. Figure 11a shows a significant reduction of thermal conductivity in $ZrNi_{1.04}Sn$ compared to the ZrNiSn[8] in the entire temperature range. Further, it is observed that the thermal conductivity is increased with Ge-doping at RT, except for 1.5 and 2.0 atom % Ge-doped $ZrNi_{1.04}Sn$ samples. However, the behavior of thermal conductivity with temperature does not follow any specific trend in all of the samples. Furthermore, it is clear from Figure 11a that the thermal conductivity of $ZrNi_{1.04}Sn_{0.98}Ge_{0.02}$ is the lowest among all of the samples in the entire temperature range.

To understand the thermal conductivity in more detail, we have separated lattice (κ_l) and electronic thermal conductivity (κ_e) from total thermal conductivity, for which κ_e was calculated using the relation $\kappa_e = L\sigma T$, known as the Wiedemann−Franz law, where the Lorenz number L was calculated using the SPB model considering scattering by acoustic phonons[45,46]

$$L = \left(\frac{k_B}{e}\right)^2 \frac{3F_0(\eta)F_2(\eta) - 4F_1^2(\eta)}{F_0^2(\eta)}$$

Electronic thermal conductivity is given in the inset of Figure 11b, which shows an increasing trend with increasing temperature, and exhibits high κ_e in $ZrNi_{1.04}Sn$ with respect to ZrNiSn.[8] The enhancement in κ_e of all of the Ge-doped $ZrNi_{1.04}Sn$ samples at ∼873 K is obtained relative to that of $ZrNi_{1.04}Sn$.

Figure 11b represents the lattice thermal conductivity κ_l, which decreases with temperature for all of the samples. Initially, it decreases slowly, and then above ∼650 K, a significant reduction is observed. Further, the lattice thermal conductivity of $ZrNi_{1.04}Sn$ is lower than ZrNiSn,[8] which may be attributed to the scattering of phonons having a wide range of wavelength via all scale hierarchical structural defects, including the grain boundary of the HH matrix and secondary phases, as well as point defects that emerged due to interstitial Ni defects. Further, Ge-doped samples exhibit high κ_l at RT except for two samples having Ge concentrations of 1.5 and 2.0 atom %. At a high temperature of ∼873 K, 0.5 atom % Ge-doped sample also exhibits lower κ_l along with 1.5 and 2.0 atom %, when compared with $ZrNi_{1.04}Sn$. This kind of abnormal behavior has also been previously observed.[40,51] Here, it is worth noting that we have observed quite different results from that expected. In general, it is assumed that the inclusion of impurity atoms improves phonon scattering due to generated point defects. However, in our observations referring to the entire measured temperature range, we found high κ_l of samples with 3.0 and 4.0 atom % Ge-doping than that of $ZrNi_{1.04}Sn$. Here, this anomalous behavior might be due to the variation in the existing volume fraction of secondary phases, which are metallic in nature.[40,51] Further, these results are not in good accordance with theoretical lattice thermal conductivity shown in Figure 10, as theoretical calculations have been carried out without introducing secondary phases.

The temperature-dependent figure of merit, ZT, of all of the synthesized samples is shown in Figure 11c. It is clear from Figure 11c that the ZT of $ZrNi_{1.04}Sn$ reaches up to 0.78 from 0.64 of ZrNiSn[8] at ∼873 K. Here, it is worth emphasizing that we have made this comparison due to a similar synthesis route adopted for the synthesis of $ZrNi_{1.04}Sn$ and ZrNiSn,[8] and the ZT values for ZrNiSn are very close to that reported in the available literature.[12,52,53] However, Gürth et al.[54] have achieved a ZT of ∼1 at ∼825 K in ZrNiSn processed employing a multistep route. Further, the maximum ZT of ∼1.06 at ∼873 K is achieved for the composition $ZrNi_{1.04}Sn_{0.98}Ge_{0.02}$. The comparison of the ZT with some of the reported state-of-the-art ZrNiSn-based materials is given in Figure 11d.

In addition to the TE properties, the mechanical properties of the material are equally important for the uninterrupted operation of the TE device. Therefore, we have also measured the microhardness as well as fracture toughness of all of the samples. The microhardness and fracture toughness of all of the synthesized samples along with the standard deviation is shown in Figure 12. The fracture toughness is calculated using a basic half penny model based on Vickers indentation, $K_c = 0.0752\frac{P}{c^{3/2}}$, where K_c denotes the fracture toughness, P is the indenter load, and c represents the average length of cracks

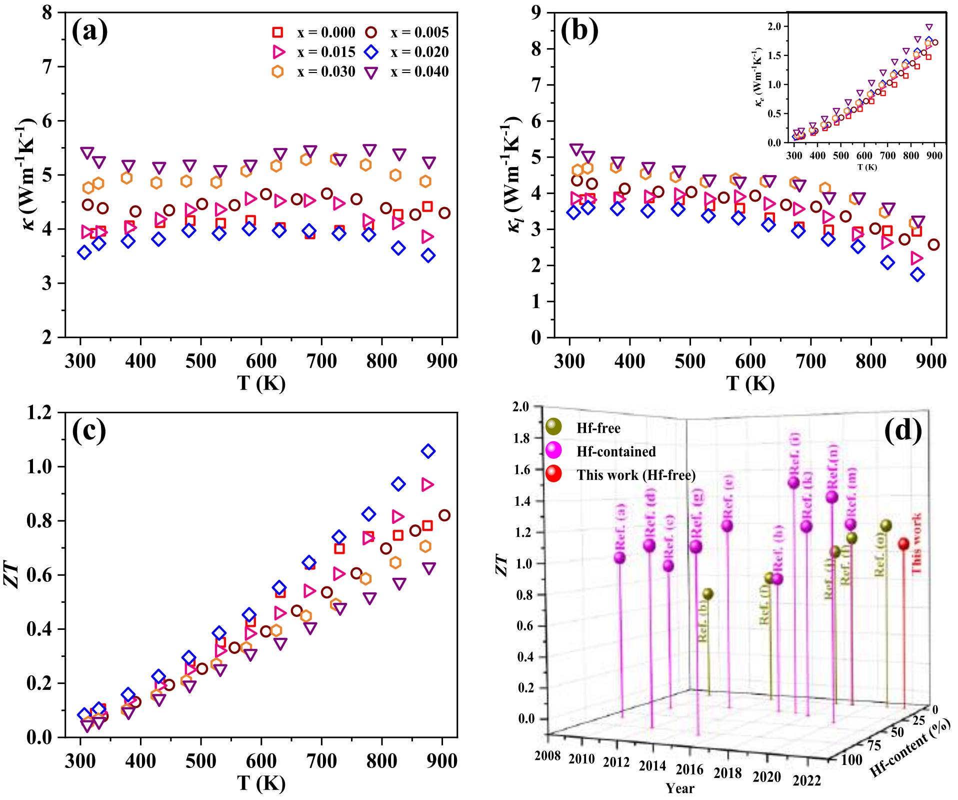

Figure 11. Temperature-dependent experimental (a) thermal conductivity, (b) lattice thermal conductivity (inset: electronic thermal conductivity), and (c) figure-of-merit (*ZT*) of $ZrNi_{1.04}Sn_{1-x}Ge_x$ ($x = 0-0.04$); (d) comparison of the *ZT* of $ZrNi_{1.04}Sn_{0.98}Ge_{0.02}$ (This work) with the literature; ref (a),[26] ref (b),[62] ref (c),[63] ref (d),[64] ref (e),[65] ref (f),[66] ref (g),[27] ref (h),[67] ref (i),[68] ref (j),[52] ref (k),[69] ref (l),[12] ref (m),[53] ref (n),[44] ref (o).[70]

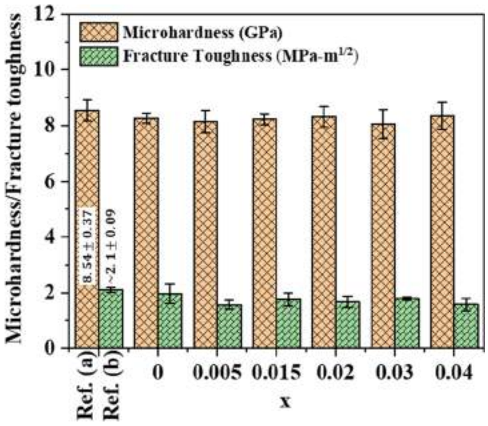

Figure 12. Microhardness and fracture toughness along with their standard deviation of $ZrNi_{1.04}Sn_{1-x}Ge_x$ ($x = 0-0.04$), and comparison with ref (a)[56] and ref (b).[57]

from the center of indentation.[55] In Figure 12, the results exhibit that all of the samples show a minor difference in microhardness as well as fracture toughness with respect to each other, and their values lie in the range 7.5−8.9 GPa for microhardness and 1.3−2.3 MPa-m$^{1/2}$ for fracture toughness, which are in good agreement with previously reported values of microhardness[56] and fracture toughness.[57] The microhardness and fracture toughness of the presented HH materials are higher than those of other TE materials.[58−61] Here, it is worth noting that the TE performance of ZrNiSn is increased in this work without penalizing mechanical properties.

5. CONCLUSIONS

In summary, two combined approaches of off-stoichiometry (Ni-excess) and isoelectronic Ge-doping were simultaneously applied in ZrNiSn. In ZrNiSn, Ni-concentration was fixed at 1.04, and Ge-concentration was varied. We realized secondary binary phase formation along with FH in ZrNiSn HH. Due to interstitial Ni, which adds intermediate bands in the band gap of ZrNiSn, and other secondary metallic phases, a maximum power factor of ~4.24 × 10^{-3} Wm^{-1} K^{-2} at ~873 K was achieved in $ZrNi_{1.04}Sn_{0.98}Ge_{0.02}$. Collectively, due to the minimal lattice thermal conductivity of ~1.75 Wm^{-1} K^{-1} and high power factor, a high *ZT* value of ~1.06 at ~873 K was attained in $ZrNi_{1.04}Sn_{0.98}Ge_{0.02}$. Further, the first-principles-based calculations provide significant insights into experimental measurements.

■ AUTHOR INFORMATION

Corresponding Authors

Sudhir Kumar − *Applied Physics Department, Faculty of Engineering and Technology, M. J. P. Rohilkhand University, Bareilly 243006, India*; Email: skumar@mjpru.ac.in
Bhasker Gahtori − *CSIR-National Physical Laboratory, New Delhi 110012, India; Academy of Scientific and Innovative Research (AcSIR), Ghaziabad 201002, India*; orcid.org/0000-0002-2222-7906; Phone: +91 11 4560 8556; Email: bhasker@nplindia.org

Authors

Kishor Kumar Johari − *CSIR-National Physical Laboratory, New Delhi 110012, India; Academy of Scientific and*

Innovative Research (AcSIR), Ghaziabad 201002, India; orcid.org/0000-0003-2240-6637

Durgesh Kumar Sharma − *Theoretical Sciences Unit, Jawaharlal Nehru Centre for Advanced Scientific Research, Bangalore 560064, India*

Ajay Kumar Verma − *CSIR-National Physical Laboratory, New Delhi 110012, India; Academy of Scientific and Innovative Research (AcSIR), Ghaziabad 201002, India*

Ruchi Bhardwaj − *CSIR-National Physical Laboratory, New Delhi 110012, India; Academy of Scientific and Innovative Research (AcSIR), Ghaziabad 201002, India*

Nagendra S. Chauhan − *Department of Materials Sciences & Engineering, IIT Kanpur, Kanpur, Uttar Pradesh 208016, India; Department of Applied Physics, Graduate School of Engineering, Tohoku University, Sendai, Miyagi 980-8579, Japan;* orcid.org/0000-0003-2579-6642

Manvendra Narayan Singh − *Synchrotrons Utilization Section, Raja Ramanna Centre for Advanced Technology, Indore 452013, India*

Sivaiah Bathula − *School of Minerals, Metallurgical and Materials Engineering, IIT Bhubaneswar, Bhubaneswar 752050, India;* orcid.org/0000-0001-6093-6351

Complete contact information is available at: https://pubs.acs.org/10.1021/acsami.2c03065

Author Contributions

K.K.J.: material synthesis, characterization, data analysis, and preparation of the first draft of the manuscript; D.K.S.: theoretical calculations and analysis; A.K.V.: mechanical properties (microhardness, fracture toughness); R.B.: material synthesis and characterization; N.S.C.: formal analysis; S.K.: theoretical calculations and analysis; M.N.S.: synchrotron XRD measurement; S.B.: FESEM imaging (higher magnification); and B.G.: conceptualization, visualization, review, and editing.

Notes

The authors declare no competing financial interest.

■ ACKNOWLEDGMENTS

The authors sincerely acknowledge the Director, CSIR-National Physical Laboratory, New Delhi, India, for providing the facilities, and K.K.J. sincerely acknowledges the financial support (31/001(0488)/2017-EMR-I) provided by CSIR-India. The authors are genuinely grateful to Radhey Shyam and Naval Kishor Upadhyay for their technical support. D.K.S. thanks the Science and Engineering Research Board (SERB) for the SERB-National Post-Doctoral Fellowship vide file number PDF/2020/002789. A.K.V. sincerely acknowledges the financial support provided by UGC, India. The authors acknowledge the Council of Scientific and Industrial Research-Fourth Paradigm Institute (CSIR-4PI) at Bengaluru.

■ REFERENCES

(1) Poon, S. J. Half Heusler compounds: promising materials for mid-to-high temperature thermoelectric conversion. *J. Phys. D: Appl. Phys.* **2019**, *52*, No. 493001.

(2) Culp, S.; Poon, S.; Sorloaica, N.; Tritt, T. In *Complex MNiSn Phases as Stable High-Temperature Thermoelectric Materials*, ICT 2005. 24th International Conference on Thermoelectrics; IEEE, 2005; pp 384−387.

(3) Raghuvanshi, P. R.; Mondal, S.; Bhattacharya, A. A high throughput search for efficient thermoelectric half-Heusler compounds. *J. Mater. Chem. A* **2020**, *8*, 25187−25197.

(4) Romaka, V.; Rogl, G.; Grytsiv, A.; Rogl, P. Determination of structural disorder in Heusler-type phases. *Comput. Mater. Sci.* **2020**, *172*, No. 109307.

(5) Barczak, S. A.; Halpin, J. E.; Buckman, J.; Decourt, R.; Pollet, M.; Smith, R. I.; MacLaren, D. A.; Bos, J.-W. G. Grain-by-Grain Compositional Variations and Interstitial Metals − A New Route toward Achieving High Performance in Half-Heusler Thermoelectrics. *ACS Appl. Mater. Interfaces* **2018**, *10*, 4786−4793.

(6) Zhao, D.; Zuo, M.; Wang, Z.; Teng, X.; Geng, H. Synthesis and thermoelectric properties of tantalum-doped ZrNiSn half-Heusler alloys. *Funct. Mater. Lett.* **2014**, *07*, No. 1450032.

(7) Akram, R.; Zhang, Q.; Yang, D.; Zheng, Y.; Yan, Y.; Su, X.; Tang, X. Enhanced thermoelectric properties of La-doped ZrNiSn half-Heusler compound. *J. Electron. Mater.* **2015**, *44*, 3563−3570.

(8) Johari, K. K.; Bhardwaj, R.; Chauhan, N. S.; Gahtori, B.; Bathula, S.; Auluck, S.; Dhakate, S. Band Structure Modification and Mass Fluctuation Effects of Isoelectronic Germanium-Doping on Thermoelectric Properties of ZrNiSn. *ACS Appl. Energy Mater.* **2020**, *3*, 1349−1357.

(9) Bahrami, A.; Ying, P.; Wolff, U.; Rodriguez, N. P.; Schierning, G.; Nielsch, K.; He, R. Reduced Lattice Thermal Conductivity for Half-Heusler ZrNiSn through Cryogenic Mechanical Alloying. *ACS Appl. Mater. Interfaces* **2021**, *13*, 38561−38568.

(10) Liu, Y.; Sahoo, P.; Makongo, J. P.; Zhou, X.; Kim, S.-J.; Chi, H.; Uher, C.; Pan, X.; Poudeu, P. F. Large enhancements of thermopower and carrier mobility in quantum dot engineered bulk semiconductors. *J. Am. Chem. Soc.* **2013**, *135*, 7486−7495.

(11) Huang, X.; Xu, Z.; Chen, L. The thermoelectric performance of ZrNiSn/ZrO2 composites. *Solid State Commun.* **2004**, *130*, 181−185.

(12) Chauhan, N. S.; Bathula, S.; Gahtori, B.; Mahanti, S. D.; Bhattacharya, A.; Vishwakarma, A.; Bhardwaj, R.; Singh, V. N.; Dhar, A. Compositional Tailoring for Realizing High Thermoelectric Performance in Hafnium-Free n-Type ZrNiSn Half-Heusler Alloys. *ACS Appl. Mater. Interfaces* **2019**, *11*, 47830−47836.

(13) Chai, Y. W.; Oniki, T.; Kimura, Y. Microstructure and thermoelectric properties of a ZrNi1. 1Sn half-Heusler alloy. *Acta Mater.* **2015**, *85*, 290−300.

(14) Makongo, J. P.; Misra, D. K.; Zhou, X.; Pant, A.; Shabetai, M. R.; Su, X.; Uher, C.; Stokes, K. L.; Poudeu, P. F. Simultaneous large enhancements in thermopower and electrical conductivity of bulk nanostructured half-Heusler alloys. *J. Am. Chem. Soc.* **2011**, *133*, 18843−18852.

(15) Bhardwaj, A.; Chauhan, N.; Sancheti, B.; Pandey, G.; Senguttuvan, T.; Misra, D. Panoscopically optimized thermoelectric performance of a half-Heusler/full-Heusler based in situ bulk composite Zr 0.7 Hf 0.3 Ni 1+ x Sn: an energy and time efficient way. *Phys. Chem. Chem. Phys.* **2015**, *17*, 30090−30101.

(16) Do, D. T.; Mahanti, S. D.; Pulikkoti, J. J. Electronic structure of Zr−Ni−Sn systems: role of clustering and nanostructures in half-Heusler and Heusler limits. *J. Phys.: Condens. Matter* **2014**, *26*, No. 275501.

(17) Chauhan, N. S.; Gahtori, B.; Sivaiah, B.; Mahanti, S. D.; Dhar, A.; Bhattacharya, A. Modulating the lattice dynamics of n-type Heusler compounds via tuning Ni concentration. *Appl. Phys. Lett.* **2018**, *113*, No. 013902.

(18) Romaka, V.; Rogl, P.; Romaka, L.; Stadnyk, Y.; Grytsiv, A.; Lakh, O.; Krayovskii, V. Peculiarities of structural disorder in Zr-and Hf-containing Heusler and half-Heusler stannides. *Intermetallics* **2013**, *35*, 45−52.

(19) Li, X.; Yang, P.; Wang, Y.; Zhang, Z.; Qin, D.; Xue, W.; Chen, C.; Huang, Y.; Xie, X.; Wang, X.; et al. Phase Boundary Mapping in ZrNiSn Half-Heusler for Enhanced Thermoelectric Performance. *Research* **2020**, *2020*, No. 4630948.

(20) Yonggang, G. Y.; Zhang, X.; Zunger, A. Natural off-stoichiometry causes carrier doping in half-Heusler filled tetrahedral structures. *Phys. Rev. B: Condens. Matter Mater. Phys.* **2017**, *95*, No. 085201.

(21) Guzik, M. N.; Echevarria-Bonet, C.; Riktor, M. D.; Carvalho, P. A.; Gunnæs, A. E.; Sørby, M. H.; Hauback, B. C. Half-Heusler phase

formation and Ni atom distribution in M-Ni-Sn (M= Hf, Ti, Zr) systems. *Acta Mater.* **2018**, *148*, 216−224.

(22) Yang, X.; Jiang, Z.; Li, J.; Kang, H.; Liu, D.; Yang, F.; Chen, Z.; Guo, E.; Jiang, X.; Wang, T. Identification of the Intrinsic Atomic Disorder in ZrNiSn-based Alloys and Their Effects on Thermoelectric Properties. *Nano Energy* **2020**, *78*, No. 105372.

(23) Wang, F.; Fukuhara, T.; Maezawa, K.; Masubuchi, S. Mn doping in half-Heusler semiconductors: Microstructural and transport properties. *Jpn. J. Appl. Phys.* **2010**, *49*, No. 053002.

(24) Sauerschnig, P.; Grytsiv, A.; Vrestal, J.; Romaka, V. V.; Smetana, B.; Giester, G.; Bauer, E.; Rogl, P. On the constitution and thermodynamic modelling of the system Zr-Ni-Sn. *J. Alloys Compd.* **2018**, *742*, 1058−1082.

(25) Shen, Q.; Chen, L.; Goto, T.; Hirai, T.; Yang, J.; Meisner, G.; Uher, C. Effects of partial substitution of Ni by Pd on the thermoelectric properties of ZrNiSn-based half-Heusler compounds. *Appl. Phys. Lett.* **2001**, *79*, 4165−4167.

(26) Yu, C.; Zhu, T.-J.; Shi, R.-Z.; Zhang, Y.; Zhao, X.-B.; He, J. High-performance half-Heusler thermoelectric materials Hf1− x ZrxNiSn1− ySby prepared by levitation melting and spark plasma sintering. *Acta Mater.* **2009**, *57*, 2757−2764.

(27) Liu, Y.; Xie, H.; Fu, C.; Snyder, G. J.; Zhao, X.; Zhu, T. Demonstration of a phonon-glass electron-crystal strategy in (Hf, Zr) NiSn half-Heusler thermoelectric materials by alloying. *J. Mater. Chem. A* **2015**, *3*, 22716−22722.

(28) Gong, B.; Liu, F.; Zhu, J.; Wang, X.; Ao, W.; Zhang, C.; Li, Y.; Li, J.; Xie, H. Effects of Sc, Ti, Hf, V, Nb and Ta doping on the properties of ZrNiSn alloys. *J. Mater. Sci.* **2019**, *54*, 10325−10334.

(29) Mallick, M. M.; Rajput, K.; Vitta, S. Increasing figure-of-merit of ZrNiSn half-Heusler alloy by minimal substitution and thermal conductivity reduction. *J. Mater. Sci.: Mater. Electron.* **2019**, *30*, 6139−6147.

(30) Johari, K. K.; Bhardwaj, R.; Chauhan, N. S.; Bathula, S.; Auluck, S.; Dhakate, S.; Gahtori, B. High thermoelectric performance in n-type degenerate ZrNiSn-based half-heusler alloys driven by enhanced weighted mobility and lattice anharmonicity. *ACS Appl. Energy Mater.* **2021**, *4*, 3393−3403.

(31) Birkel, C. S.; Douglas, J. E.; Lettiere, B. R.; Seward, G.; Verma, N.; Zhang, Y.; Pollock, T. M.; Seshadri, R.; Stucky, G. D. Improving the thermoelectric properties of half-Heusler TiNiSn through inclusion of a second full-Heusler phase: microwave preparation and spark plasma sintering of TiNi 1+ x Sn. *Phys. Chem. Chem. Phys.* **2013**, *15*, 6990−6997.

(32) Kresse, G.; Furthmüller, J. Efficient iterative schemes for ab initio total-energy calculations using a plane-wave basis set. *Phys. Rev. B: Condens. Matter Mater. Phys.* **1996**, *54*, 11169.

(33) Perdew, J. P.; Burke, K.; Ernzerhof, M. Generalized gradient approximation made simple. *Phys. Rev. Lett.* **1996**, *77*, 3865.

(34) Perdew, J. P.; Burke, K.; Ernzerhof, M. Erratum: generalized gradient approximation made simple. *Phys. Rev. Lett* **1997**, *78*, 1396.

(35) Armiento, R.; Mattsson, A. E. Functional designed to include surface effects in self-consistent density functional theory. *Phys. Rev. B: Condens. Matter Mater. Phys.* **2005**, *72*, No. 085108.

(36) Mattsson, A. E.; Armiento, R. Implementing and testing the AM05 spin density functional. *Phys. Rev. B: Condens. Matter Mater. Phys.* **2009**, *79*, No. 155101.

(37) Mattsson, A. E.; Armiento, R.; Paier, J.; Kresse, G.; Wills, J. M.; Mattsson, T. R. The AM05 density functional applied to solids. *J. Chem. Phys.* **2008**, *128*, No. 084714.

(38) Togo, A.; Tanaka, I. First principles phonon calculations in materials science. *Scr. Mater.* **2015**, *108*, 1−5.

(39) Sinha, A.; Sagdeo, A.; Gupta, P.; Upadhyay, A.; Kumar, A.; Singh, M.; Gupta, R.; Kane, S.; Verma, A.; Deb, S. *Angle Dispersive X-ray diffraction Beamline on Indus-2 Synchrotron Radiation Source: Commissioning and First Results*, Journal of Physics: Conference Series; IOP Publishing, 2013; p 072017.

(40) Chetty, R.; Bali, A.; Femi, O.; Chattopadhyay, K.; Mallik, R. Thermoelectric properties of in-doped Cu2ZnGeSe4. *J. Electron. Mater.* **2016**, *45*, 1625−1632.

(41) Miyazaki, H.; Nakano, T.; Inukai, M.; Soda, K.; Izumi, Y.; Muro, T.; Kim, J.; Takata, M.; Matsunami, M.; Kimura, S.-i.; et al. Electronic and local crystal structures of the ZrNiSn half-Heusler thermoelectric material. *Mater. Trans.* **2014**, *55*, 1209−1214.

(42) Misra, D.; Bhardwaj, A.; Singh, S. Enhanced thermoelectric performance of a new half-Heusler derivative Zr 9 Ni 7 Sn 8 bulk nanocomposite: enhanced electrical conductivity and low thermal conductivity. *J. Mater. Chem. A* **2014**, *2*, 11913−11921.

(43) Page, A.; Poudeu, P.; Uher, C. A first-principles approach to half-Heusler thermoelectrics: Accelerated prediction and understanding of material properties. *J. Materiomics* **2016**, *2*, 104−113.

(44) Chauhan, N. S.; Raghuvanshi, P. R.; Tyagi, K.; Johari, K. K.; Tyagi, L.; Gahtori, B.; Bathula, S.; Bhattacharya, A.; Mahanti, S. D.; Singh, V. N.; et al. Defect Engineering for Enhancement of Thermoelectric Performance of (Zr, Hf) NiSn-Based n-type Half-Heusler Alloys. *J. Phys. Chem. C* **2020**, *124*, 8584−8593.

(45) May, A. F.; Snyder, G. J. Introduction to modeling thermoelectric transport at high temperatures. *Materials, Preparation, and Characterization in Thermoelectrics*; CRC press, 2017; pp 207−224.

(46) Naithani, H.; Dasgupta, T. Critical analysis of single band modeling of thermoelectric materials. *ACS Appl. Energy Mater.* **2020**, *3*, 2200−2213.

(47) Lan, J.-L.; Zhan, B.; Liu, Y.-C.; Zheng, B.; Liu, Y.; Lin, Y.-H.; Nan, C.-W. Doping for higher thermoelectric properties in p-type BiCuSeO oxyselenide. *Appl. Phys. Lett.* **2013**, *102*, No. 123905.

(48) Hu, L.; Fang, Y.-W.; Qin, F.; Cao, X.; Zhao, X.; Luo, Y.; Repaka, D. V. M.; Luo, W.; Suwardi, A.; Soldi, T. High thermoelectric performance enabled by convergence of nested conduction bands in Pb7Bi4Se13 with low thermal conductivity. *Nat. Commun.* **2021**, *12*, No. 4793.

(49) Saparamadu, U.; De Boor, J.; Mao, J.; Song, S.; Tian, F.; Liu, W.; Zhang, Q.; Ren, Z. Comparative studies on thermoelectric properties of p-type Mg2Sn0. 75Ge0. 25 doped with lithium, sodium, and gallium. *Acta Mater.* **2017**, *141*, 154−162.

(50) Berland, K.; Shulumba, N.; Hellman, O.; Persson, C.; Løvvik, O. M. Thermoelectric transport trends in group 4 half-Heusler alloys. *J. Appl. Phys.* **2019**, *126*, No. 145102.

(51) Huang, L.; Wang, J.; Chen, X.; He, R.; Shuai, J.; Zhang, J.; Zhang, Q.; Ren, Z. The effects of excess Co on the phase composition and thermoelectric properties of half-Heusler NbCoSb. *Materials* **2018**, *11*, 773.

(52) Chauhan, N. S.; Bathula, S.; Vishwakarma, A.; Bhardwaj, R.; Gahtori, B.; Kumar, A.; Dhar, A. Vanadium-doping-induced resonant energy levels for the enhancement of thermoelectric performance in Hf-free ZrNiSn half-Heusler alloys. *ACS Appl. Energy Mater.* **2018**, *1*, 757−764.

(53) Gong, B.; Li, Y.; Liu, F.; Zhu, J.; Wang, X.; Ao, W.; Zhang, C.; Li, J.; Xie, H.; Zhu, T. Continuously enhanced structural disorder to suppress the lattice thermal conductivity of ZrNiSn-based half-Heusler alloys by multielement and multisite alloying with very low Hf content. *ACS Appl. Mater. Interfaces* **2019**, *11*, 13397−13404.

(54) Gürth, M.; Rogl, G.; Romaka, V.; Grytsiv, A.; Bauer, E.; Rogl, P. Thermoelectric high ZT half-Heusler alloys Ti1− x− yZrxHfyNiSn (0≤ x≤ 1; 0≤ y≤ 1). *Acta Mater.* **2016**, *104*, 210−222.

(55) Moradkhani, A.; Baharvandi, H.; Tajdari, M.; Latifi, H.; Martikainen, J. Determination of fracture toughness using the area of micro-crack tracks left in brittle materials by Vickers indentation test. *J. Adv. Ceram.* **2013**, *2*, 87−102.

(56) Fan, X. *Mechanical Characterization of Hydroxyapatite, Thermoelectric Materials and Doped Ceria*; Michigan State University. Materials Science and Engineering, 2013.

(57) Rogl, G.; Grytsiv, A.; Gürth, M.; Tavassoli, A.; Ebner, C.; Wünschek, A.; Puchegger, S.; Soprunyuk, V.; Schranz, W.; Bauer, E.; et al. Mechanical properties of half-Heusler alloys. *Acta Mater.* **2016**, *107*, 178−195.

(58) Zhao, L.-D.; Zhang, B.-P.; Li, J.-F.; Zhou, M.; Liu, W.-S.; Liu, J. Thermoelectric and mechanical properties of nano-SiC-dispersed

Bi2Te3 fabricated by mechanical alloying and spark plasma sintering. *J. Alloys Compd.* **2008**, *455*, 259−264.

(59) Schmidt, R. D.; Fan, X.; Case, E. D.; Sarac, P. B. Mechanical properties of Mg 2 Si thermoelectric materials with the addition of 0−4 vol% silicon carbide nanoparticles (SiC NP). *J. Mater. Sci.* **2015**, *50*, 4034−4046.

(60) He, R.; Gahlawat, S.; Guo, C.; Chen, S.; Dahal, T.; Zhang, H.; Liu, W.; Zhang, Q.; Chere, E.; White, K.; Ren, Z. Studies on mechanical properties of thermoelectric materials by nanoindentation. *Phys. Status Solidi A* **2015**, *212*, 2191−2195.

(61) Gelbstein, Y.; Tunbridge, J.; Dixon, R.; Reece, M. J.; Ning, H.; Gilchrist, R.; Summers, R.; Agote, I.; Lagos, M. A.; Simpson, K.; et al. Physical, mechanical, and structural properties of highly efficient nanostructured n-and p-silicides for practical thermoelectric applications. *J. Electron. Mater.* **2014**, *43*, 1703−1711.

(62) Katsuyama, S.; Kobayashi, T. Effect of mechanical milling on thermoelectric properties of half-Heusler ZrNiSn0. 98Sb0. 02 intermetallic compound. *Mater. Sci. Eng., B* **2010**, *166*, 99−103.

(63) Lee, P.-J.; Tseng, S. C.; Chao, L.-S. High-temperature thermoelectric properties of Tix (ZrHf) 0.99− xV0. 01Ni0. 9Pd0. 1Sn0. 99Sb0. 01 half-Heusler alloys. *J. Alloys Compd.* **2010**, *496*, 620−623.

(64) Bhardwaj, A.; Misra, D.; Pulikkotil, J.; Auluck, S.; Dhar, A.; Budhani, R. Implications of nanostructuring on the thermoelectric properties in half-Heusler alloys. *Appl. Phys. Lett.* **2012**, *101*, No. 133103.

(65) Schwall, M.; Balke, B. Phase separation as a key to a thermoelectric high efficiency. *Phys. Chem. Chem. Phys.* **2013**, *15*, 1868−1872.

(66) Xie, H.; Wang, H.; Fu, C.; Liu, Y.; Snyder, G. J.; Zhao, X.; Zhu, T. The intrinsic disorder related alloy scattering in ZrNiSn half-Heusler thermoelectric materials. *Sci. Rep.* **2014**, *4*, No. 6888.

(67) Akram, R.; Yan, Y.; Yang, D.; She, X.; Zheng, G.; Su, X.; Tang, X. Microstructure and thermoelectric properties of Sb doped Hf0. 25Zr0. 75NiSn Half-Heusler compounds with improved carrier mobility. *Intermetallics* **2016**, *74*, 1−7.

(68) Rogl, G.; Sauerschnig, P.; Rykavets, Z.; Romaka, V.; Heinrich, P.; Hinterleitner, B.; Grytsiv, A.; Bauer, E.; Rogl, P. (V, Nb)-doped half Heusler alloys based on {Ti, Zr, Hf} NiSn with high ZT. *Acta Mater.* **2017**, *131*, 336−348.

(69) Chauhan, N. S.; Bathula, S.; Vishwakarma, A.; Bhardwaj, R.; Johari, K. K.; Gahtori, B.; Saravanan, M.; Dhar, A. Compositional tuning of ZrNiSn half-Heusler alloys: Thermoelectric characteristics and performance analysis. *J. Phys. Chem. Solids* **2018**, *123*, 105−112.

(70) Van Du, N.; Nam, W. H.; Cho, J. Y.; Binh, N. V.; Huy, P. T.; Tuan, D. A.; Shin, W. H.; Lee, S. Enhanced thermoelectric properties of Hf-free half-Heusler compounds prepared via highly fast process. *J. Alloys Compd.* **2021**, *886*, No. 161293.